Dual defect regulation of BiOCl halogen layer enables photocatalytic O_2 activation into singlet oxygen for refractory aromatic pollutant removal

Yandong Sun [a], Weiguang Han [a], Fangyuan Zhang [a], Hui Li [b], Ziqi Zhang [a], Xue Zhang [a], Boxiong Shen [a], Sheng-Qi Guo [a,c,*], Tianyi Ma [b,**]

[a] *Tianjin Key Laboratory of Clean Energy and Pollutant Control, School of Energy and Environmental Engineering, Hebei University of Technology, Tianjin 300401, China*
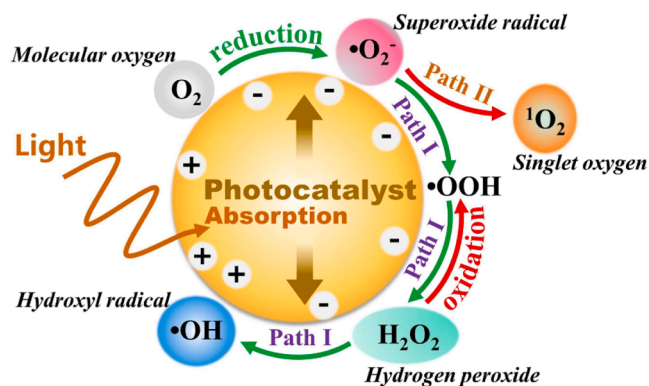[b] *School of Science, STEM College, RMIT University, Melbourne, VIC 3000, Australia*
[c] *Department of Food and Chemical Engineering, Liuzhou Institute of Technology, Liuzhou, Guangxi 545616, China*

A R T I C L E   I N F O

A B S T R A C T

The generation of singlet oxygen ($^1O_2$) based on photocatalytic activation O_2 is considered to have important application prospects in purifying refractory organic pollutants in water. However, the uncertain dual pathway transformation of activated O_2 severely limits the generation of $^1O_2$. In this work, we show a robust BiOCl with dual defects (adjacent I-substitution defect and Cl vacancy) in halogen layer for the selective activation of O_2 to generate $^1O_2$. Combining experiments and theoretical calculations, we confirm that dual defects are beneficial in optimizing band structures, improving carrier separation efficiency, and promoting O_2 adsorption and activation. More importantly, it is confirmed that dual defects can directionally convert O_2 into $^1O_2$ by increasing the thermodynamic conversion energy barrier of non-$^1O_2$ conversion pathways and serving as a necessary site for $^1O_2$ generation with dual functions of oxidation and reduction. Applying dual defect modified BiOCl to the removal of refractory aromatic pollutants in water, it is found that it has efficient and stable photocatalytic degradation efficiency and broad environmental adaptability. This work not only provides in-depth insights into the mechanism of photocatalytic activation of O_2 to selective produce $^1O_2$, but also lays the foundation for further development of highly active photocatalysts for environmental remediation and energy conversion.

1. Introduction

Oxygen (O_2) in the atmosphere is the most environmentally friendly oxidant, providing the possibility for benign environmental remediation [1,2]. However, O_2 is hardly to directly oxidize pollutants under ambient conditions due to the restriction of electron spin forbidden effect [3,4]. To address this issue, some artificial O_2 activation strategies have been proposed, including construction of enzymes and metalloporphyrin activation systems, which, however, the harsh synthesis conditions and expensive prices limit its promotion and application [5–8]. In comparison, photocatalytic oxidation (PCO) technology driven by solar energy provides a more promising pathway. In PCO reaction, photo-generated electrons can combine with O_2 adsorbed on the surface of catalyst to form superoxide radicals ($\bullet O_2$), which can be further oxidized or reduced to various reactive oxygen species (ROS), such as

hydroxyl radicals ($\bullet OH$), hydrogen peroxide (H_2O_2) and singlet oxygen ($^1O_2$) (Scheme 1) [9–11].

With the continuous deepening of understanding the properties of $^1O_2$, it has gradually become a new darling in the field of environmental remediation applications, especially in the treatment of refractory organic pollutants in water. $^1O_2$ with mild oxidation ability (2.2 eV vs NHE) can selectively oxidize unsaturated organics through electrophilic addition and electron abstraction reactions, which makes it become an effective ROS to remove aromatic organic pollutants from water [12–14]. Compared to widely studied $\bullet O_2$ and $\bullet OH$, $^1O_2$ has a higher tolerance to water matrixes and a relatively long lifetime (over an hour in gas phase and 10^{-6} - 10^{-3} s in solution), which enables it to persistently deep mineralization pollutants in complex water quality environments, and suppressing the production of undesirable degradation byproducts [15,16]. The attractive characteristics stimulate people's

---

Scheme 1. The adsorption and activation process of O_2 on the catalyst surface.

passion for exploring the controllable production of $^1O_2$. For a long time, the effective spatial separation of photo-generated electrons and holes is considered to be the key to achieving efficient photocatalytic performance and a prerequisite for harvesting $^1O_2$ [17–19]. This requires that the electrons can combine with the adsorbed O_2 on the catalyst surface before recombination with holes in the bulk. In order to shorten the distance of bulk electron migration to the surface, layered two-dimensional (2D) photocatalysts with low spatial dimensions become popular [20–22].

Although the development of 2D photocatalysts (such as BiOX (X = Cl, Br, I), MoS_2 and WS_2) has greatly improved the photocatalytic activation efficiency of O_2, the generation of $^1O_2$ is still limited by the irregular dual pathway conversion of $\bullet O_2^-$. After the formation of $\bullet O_2^-$, it may continue to combine with electrons and undergo a series of reduction reactions to generate intermediate species, including $\bullet OOH$, H_2O_2 and $\bullet OH$ (pathway I); it is also possible to form $^1O_2$ by hole oxidation through another pathway (II) [23–25]. Unfortunately, compared to pathway I, the occurrence of path II usually requires more additional energy, which increases the difficulty of the reaction [26]. More importantly, O_2 commonly adsorbed in the high electron density regions and subjected to continuous electron attacks, which makes it difficult for $\bullet O_2^-$ to combine with holes, resulting in the transformation of pathway II is inhibited [27,28]. The urgent need is to adjust the single charge attribute of O_2 activation sites, and establish a hole aggregation island within the electron enrichment region to facilitate oxidation reaction with $\bullet O_2^-$ and induce $^1O_2$ selective generation. At present, the design concept of high-yield $^1O_2$ photocatalysts still focuses on enhancing the separation efficiency of photo-generated charges and increasing O_2 adsorption capacity, aiming to increase the concentration of $\bullet O_2^-$ and harvest more $^1O_2$ [29]. There has not yet been any research centering on the selective optimization of $\bullet O_2^-$ conversion pathways, and related research undoubtedly helps guide the design concept of high-yield $^1O_2$ photocatalysts to a higher level.

Here, we developed an effective strategy to regulate the selective conversion of $\bullet O_2^-$ to $^1O_2$ in layered 2D photocatalysts: construction of dual defect active sites. Typical 2D BiOCl was chose as research model due to its layered structure interleaved with $[Bi_2O_2]$ slabs and double halogenated atoms slabs, which provide convenience for identifying the characteristics of defect structures and analyzing functionality. Introduce dual defect (adjacent I-substitution defect and Cl vacancy) into surface halogen layer through a simple method. Experimental and theoretical calculation results indicate that dual defects not only improve the efficiency of photo-generated charge separation but also promote the adsorption of O_2. More important, dual defects effectively enhance the thermodynamic energy barrier of reaction pathway I, requiring more energy than pathway II. Meanwhile, dual defects provide double sites for the redox reaction of O_2 and achieve selective conversion of $\bullet O_2^-$ to $^1O_2$ by adjusting the adsorption configuration of O_2. We also demonstrate that in both deionized water and complex water

quality environments, these dual defects can enhance the rapid and complete degradation of refractory aromatic pollutant. This new approach may advance the design of highly efficient photocatalysts.

2. Experimental

2.1. Materials and fabrication

All reagents used in this research were purchased from Aladdin (analytical grade) and used without further purification. BiOCl nanosheets were synthesized by a simple solvothermal method. Specifically, dissolve $Bi(NO_3)_3 \cdot 5\ H_2O$ (1.0 mmol, 0.485 g) and polyvinylpyrrolidone (0.400 g) in mannitol (25 mL, 0.10 M), and stirring for 30 min. Then, slowly add KCl solution (1.0 mmol) to the solution and continue stirring for 10 min. Subsequently, the suspension was transferred into a Teflon autoclave with a capacity of 50 mL and then kept at 160 °C for 3 h. After the reaction is completed, solid precipitates are obtained through steps including cooling and washing, and then dried to form BiOCl nanosheets, labeled as BOC. BiOCl nanosheets with Cl vacancies were obtained by photolithography of BOC. Disperse 0.20 g BOC in 50 mL aqueous solution, irradiate with UV ($\lambda \le 400$ nm) for 50 min, then wash and dry to obtain a solid powder, named BOC-V_{Cl}.

The synthesis method of BiOCl nanosheets with I-substitution defects (labeled as BOC-D_I) is the same as that of BOC, except that the KCl solution was replaced with a mixed solution of KCl and KI, with the total amount added unchanged. BiOCl nanosheets with dual defects (labeled as BOC-$D_I V_{Cl}$) were obtained by photolithography of BOC-D_I. The method of photolithography is same as BOC-V_{Cl}.

2.2. Material characterizations

The surface functional groups of the samples were determined by FT-IR spectra (Frontier Mid-IR FTIR). Crystal phase structure was characterized by X-ray diffraction (XRD) patterns (Shimadzu XRD-6100) with Cu Ka radiation ($\lambda = 1.54056$ Å). Surface structure and elemental composition was detected using X-ray photoelectron spectroscopy (XPS, phi-5700 ESCA). Confirming that the elements of detached atoms in photo-etching was undertaken by ion chromatography (IC) technique (Thermo Scientific Dionex Aquion IC). Atomic force microscopy (AFM) images were recorded on a Bruker Atomic Force Microscope under trapping-mode. The morphology of the samples was observed by scanning electron microscopy (SEM, Nova Nano SEM 460, FEI) and transmission electron microscopy (TEM, Talos F200X, FEI). Elemental mapping was verified by TEM-energy dispersive X-ray (EDS) detector system. Atomic ratio of each element in catalysts was determined by Electron Probe X-ray Micro-Analyzer (EPMA, JXA-8530 F Plus). Pore structure and surface area were established by Quantachrome Nova 4000a analyzer. Electron paramagnetic resonance (ESR, EMXplus-6/1) characterizes chlorine vacancies and reactive oxygen species (ROS), and Raman spectroscopy (HORIBA JOBIN YVON S.A.S., EVOLUTION, Germany) further analyzes the presence of chlorine vacancies. UV-Vis absorption spectroscopy (Lambda 750 UV/VIS/NIR) was used to analyze the light response characteristics of samples. Photoluminescence spectra (PL, Jobin Yvon Fluorolog 3-TAU spectrofluorimeter) and surface photovoltage (SPV, CEL-SPS1000 surface photovoltage spectrometer) were used to characterize the separation efficiency of photogenerated charge carriers. Photocurrent density was studied by electrochemical workstation, and using a three-electrode system (Pt foil as counter electrode, saturated calomel electrode (SCE) as reference electrode and BiOCl-based samples as working electrode). The temperature-programmed desorption (TPD) of adsorption O_2 experiment was conducted by a ChemBET Pulsar TPR/TPD (Quantachrome). Electrochemical impedance spectroscopy (EIS) was performed using an impedance measurement workstation unit (frequency range from $0.1–10^6$ Hz, and sinusoidal AC perturbation of 5 mV). The charge density investigated by Mott-Schottky plots could be calculated from the

following equation [30]:

$$N_d = \frac{2}{e_0 \varepsilon \varepsilon_0 s}$$

where N_d is the charge density, e_0 is the elementary charge (1.60×10^{19} C), ε is the relative constant (taken 6.0 as BiOCl), ε_0 is the permittivity of vacuum (8.85×10^{-12} F·m^{-1}), and s represents the curve slope.

2.3. X-ray absorption fine structure data collection

The Bi L-edge X-ray absorption find structure spectra of BiOCl-based samples were recorded at 1W1B station in Beijing Synchrotron Radiation Facility (BSRF) under ambient conditions using a transmission mode. The storage ring conditions of BSRF was operated at the energy of 2.5 GeV and a maximum current of 250 mA with double-crystal Si (111) as monochromator for energy selection.

2.4. Computational details

The calculations were completed in the framework of density functional theory (DFT) with the projector augmented plane-wave method, as implemented in the Vienna ab initio simulation package [31]. The Perdew-Burke-Ernzerhof (PBE) functional with Grimme D3 correction was employed for the DFT exchange correlation energy [32]. Unrestricted Kohn-Sham DFT has been used as the electronic structure method in the framework of the Gaussian and plane waves method [33]. The Goedecker-Teter-Hutter (GTH) pseudopotentials, DZVP-MOLOPT-GTH basis sets were utilized to describe the molecules. A plane-wave energy cut-off of 500 Ry has been employed. The adsorption energy was calculated by the following equation (taking the adsorption of O_2 molecule on the substrate as an example):

$$E_{\text{ad}} = E_{\text{tot}} - E_{\text{substrate}} - E_{\text{oxygen molecule}}$$

where E_{tot} and $E_{\text{substrate}}$ are the total energies of the relaxed model with and without O_2 molecule, respectively. $E_{\text{oxygen molecule}}$ is the calculated energy of one O_2 molecule. Partial atomic charges were obtained using Bader charge analysis.

2.5. Molecular oxygen activation measurements

Aqueous suspension of the samples (50 μL, 10 g·L^{-1}) and 3,3′,5,5′-tetramethylbenzidine (TMB) (20 μL, 50 mM) were mixed with 2 mL of HAc/NaAc buffer solution. A 300 W xenon lamp equipped with a 420 nm cutoff filter was used as the light source. TMB oxidation were detected by UV-Vis measurements (the absorbance around 370 nm) at different time intervals.

2.6. Photocatalytic degradation of aromatic pollutants

The photodegradation experiment of aromatic pollutants was completed through a photochemical reactor. A 300 W xenon lamp equipped with a 420 nm cutoff filter was used as the light source. The detailed process involves dispersing 20 mg of catalyst powder into an aqueous solution containing pollutants and stirring to form a suspension. After starting the illumination, 5 mL of solution was extracted from the reactor at intervals and the catalyst was removed through the membrane. The concentration of pollutants after photocatalytic degradation was determined by high-performance liquid chromatography (HPLC). The total organic carbon (TOC) value was tested by TOC analyzer (Metash, TOC-2000).

3. Results and discussion

3.1. Structure characterization

In this work, tetragonal BiOCl is chosen as the model system, and the samples with dual defects named BOC-D$_I$V$_{Cl}$ were obtained through a two-step method of hydrothermal and photo-etching (Fig. 1a). To highlight the indispensability of dual defects, three samples were synthesized respectively as references, including a BiOCl with no defects (denoted as BOC), a BiOCl with I-substitution defects (denoted as BOC-D$_I$), and a BiOCl with Cl vacancies (denoted as BOC-V$_{Cl}$). Fig. S1 exhibits the FT-IR spectra. All of the samples display similar stretching, proving that no other new substances appeared during the modification of halogen layer. Crystal phase was determined by XRD (Fig. 1b). BOC-V$_{Cl}$ exhibits similar diffraction peaks to BOC, indicating that the photolithography process (Cl etching) did not cause changes in crystal structure. Compared to BOC, the (101) and (110) crystal facet peaks of BOC-D$_I$ and BOC-D$_I$V$_{Cl}$ shift to a smaller angle, representing that parts of Cl atoms are substituted by I atoms with a larger ionic radius [34]. Meanwhile, the position of these peaks is located in the middle of the diffraction peaks on the two crystal facets of BiOCl and BiOI, which shows that both samples are not mixtures of BiOCl and BiOI phase, but BiOCl$_n$I$_{1-n}$ ($0 < n < 1$) alloys, proving the formation of I-substitution defects. XPS (Fig. 1c) further verified the existence of I-substitution defects in BOC-D$_I$ and BOC-D$_I$V$_{Cl}$. Moreover, EPMA was used to determined atomic ratio of Cl/Bi (Fig. 1d and Table S1). It can be seen that regardless of I-substitution or photolithography, the Cl atom content in BiOCl was significantly decreased, and further photo-etching on the basis of BOC-D$_I$ also results in BOC-D$_I$V$_{Cl}$ having the lowest Cl/Bi ratio. IC was used to monitor the ions composition in the solution of BOC and BOC-D$_I$ after photo-etching, and it was confirmed that only Cl ions fallen off, revealing that photo-etching did not cause the occurrence of I vacancies (Fig. S2).

SEM (Fig. S3) and TEM images (Fig. S4) show that all the samples have the same nanosheet morphology, with a diameter around 40 nm. The information on the thickness of these nanosheets was obtained from the AFM images and the corresponding height profile. It can be seen from Fig. S5 that the thickness is around 1.5 nm, demonstrating that all the nanosheets consists of nearly 2 [Cl-Bi-O-Bi-Cl] units (7.37 Å) [35]. High resolution TEM (HR-TEM) images (Fig. 1e and S6) exhibit the spacing of continuous lattice fringes images is 0.275 nm, which agree well with the theoretical plane spacing of (110) facet perpendicular to (001) facet. The corresponding selected-area electron diffraction (SAED) pattern not only confirm the single-crystalline nature of the samples, but also disclose the angle of adjacent diffraction spots is 45°, which consists with the theoretical value of the angle between the (110) and (200) facets of tetragonal BiOCl, meaning that the set of diffraction spots can be indexed as the [001] zone axis (Fig. 1f). Thus, it can be determined that the upper and bottom exposed surfaces of the nanosheets are (001) facets of BiOCl. TEM-energy dispersive X-ray (EDS) mapping (Fig. 1g) and EDS spectrum (Fig. 1h) profiles on BOC-D$_I$V$_{Cl}$ show the distribution of Bi, O, Cl and I elements, which manifests uniform I exists. To further reveal the influence of defects on the morphology and structure of the samples, specific surface area and average pore size were investigated (Fig. S7). By comparison, it can be found that Cl vacancies benefit to increase the specific surface area of the samples, as vacancies increase the surface roughness. A larger pore size of BOC-V$_{Cl}$ confirms this point. In contrast, I-substitution defects can cause a slight decrease in specific surface area. Based on SEM images in Fig. S3, it is believed that the change is due to the increase in aggregation degree of nanosheets caused by I-substitution defects.

X-ray absorption near-edge structure (XANES) and extended X-ray absorption fine structure (EXAFS) were then used to analysis the defect structure. The Bi L-edge XANES spectra show slight difference among the samples, indicating that exist local chemical environment difference for Bi atoms (Fig. 2a). As revealed by Fourier transformed (FT) k^3-
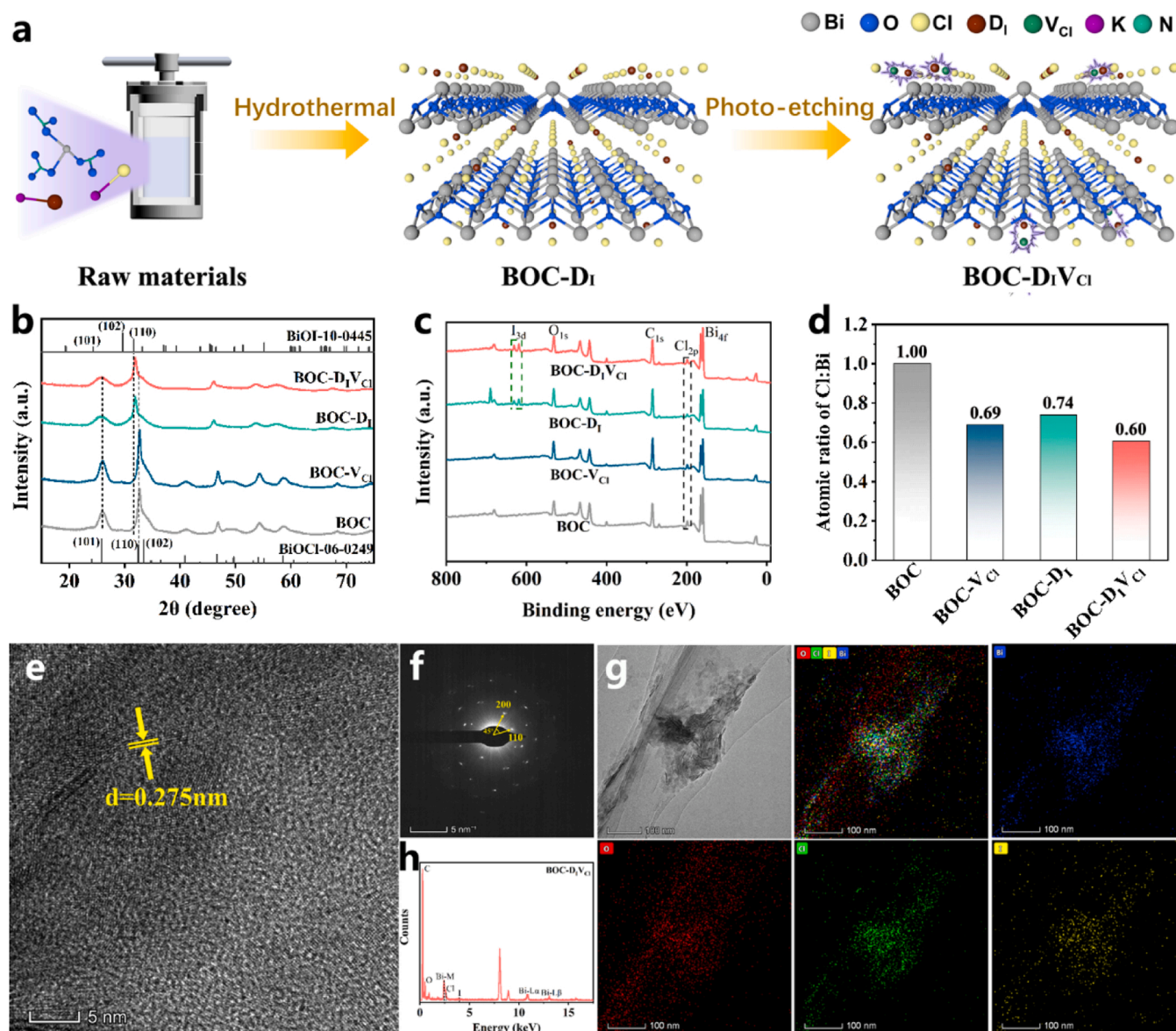
Fig. 1. (a) XRD patterns and (b) XPS spectroscopy of the samples; (c) Atom ratio of Cl/Bi of the samples, (d) TEM image, (e) HR-TEM image and (f) SAED pattern of BOC-D$_I$V$_{Cl}$; (g, h) EDS mapping and (i) EDS spectrum of BOC-D$_I$V$_{Cl}$.

weighted EXAFS spectra in Fig. 2b, two prominent peaks at the positions around 1.75 Å and 2.73 Å are attributed to Bi-O and Bi-Cl, respectively. It is found that the Bi-O peaks of the samples appeared in the same R space, indicating that the Bi-O layer has similar atomic spatial arrangement. For the position of Bi-Cl peaks, it can be seen that BOC-D$_I$ exhibits a slight lower R space than that of BOC, suggesting that there is no significant spatial arrangement change in its halogen layer, which indirectly confirms that replacing the position of Cl atom with I atom is not cause lattice distortion [36]. In comparison, BOC-D$_I$V$_{Cl}$ and BOC-V$_{Cl}$ obvious shifted to a lower R direction, ESR presenting a decrease in the average bond length of Bi-Cl bonds, which means the occurrence of Cl vacancies. Among them, the shift of Bi-Cl peak in BOC-V$_{Cl}$ is more noticeable, showing the presence of higher concentration of Cl vacancies [37].

Raman spectra (Fig. 2c) is employed to further characterize the defect structure of the samples. Two strong bands around 146 and 60 cm^{-1} in should be attributed to A_{1g} internal and external Bi-Cl stretching mode, while the band at 199 cm^{-1} is assigned to the E_g internal stretching mode [38]. The difference is that the characteristic band of Cl vacancies at 101 cm^{-1} is only observed in BOC-D$_I$V$_{Cl}$ and

BOC-V$_{Cl}$, confirming the existence of Cl vacancies [39]. ESR spectrum (Fig. 2d) also establish the existence of Cl vacancies. As well-known, the prominent signal with g value at 2.001 in BiOCl is arisen from unpaired localized electrons on Cl or O vacancies. Here, we used XPS to eliminate the interference of O vacancies before monitoring the Cl vacancies. Fig. S8 shows that the O$_{1s}$ high resolution XPS spectra of all samples can be fitted into three Gaussian peaks. Among them, the peak at 532.3 eV is attributable to the O^{2-} in O vacancies, and corresponding intensity is proportional to the concentration of O vacancies [40]. The similar peak intensities indicate that O vacancy concentrations in the samples are close, thus it can be inferred that the difference in ESR signal intensity is caused by different concentration of Cl vacancies. As expected, BOC-D$_I$V$_{Cl}$ and BOC-V$_{Cl}$ displayed higher peak intensities, further indicating the presence of Cl vacancies in their structures. It is worth noting that the concentration of Cl vacancies in BOC-V$_{Cl}$ is significantly higher than that in BOC-D$_I$V$_{Cl}$, which is consistent with the conclusion in IC chromatography, demonstrating the presence of more Cl vacancies on the surface of BOC-V$_{Cl}$. Based on the above characterization, it can be confirmed that BOC-D$_I$ has I-substitution defects, BOC-V$_{Cl}$ has Cl vacancies, while BOC-D$_I$V$_{Cl}$ possesses both I-substitution defects and Cl
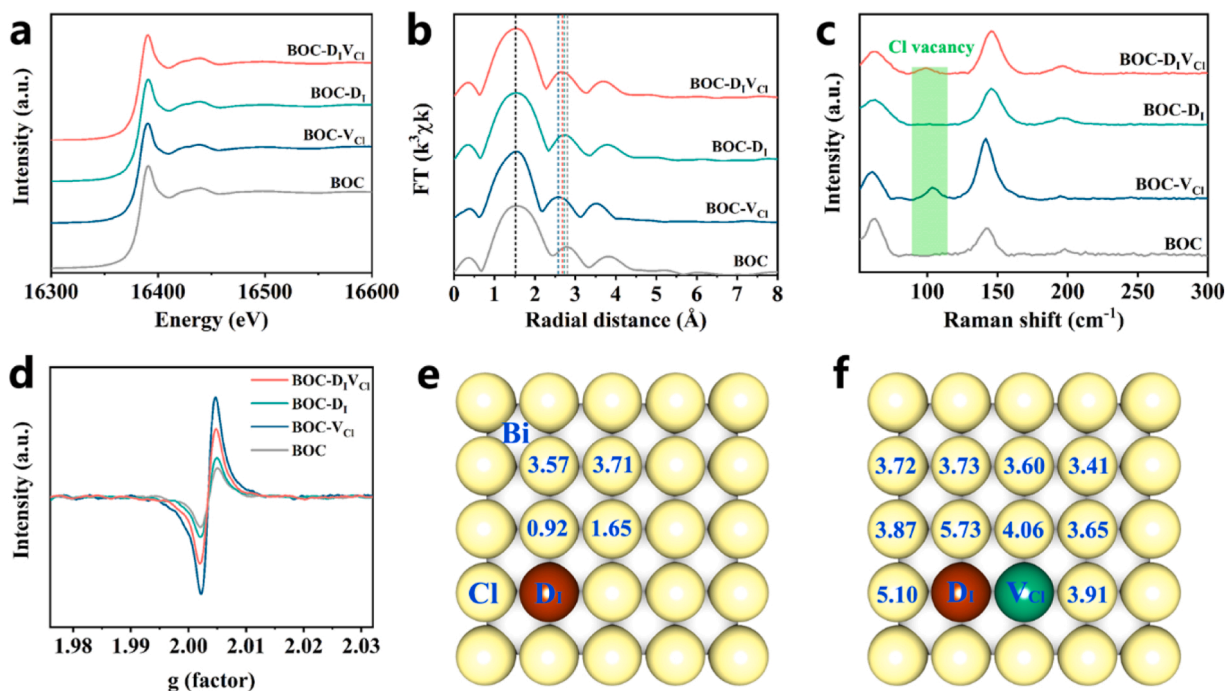
Fig. 2. (a) Bi L-edge XANES spectra and (b) FT k^3-weighted EXAFS spectra of the samples; (c) Raman spectra and (d) O vacancies ESR spectra of the samples; the formation energy of Cl vacancies at different positions on halogen layer of (e) BOC-D_I and (f) BOC-D_IV_{Cl}.

vacancies.

The positional relationship between the two types of defects in the halogen layer of BOC-D_IV_{Cl} was analyzed. According to the synthesis process, I-substitution defects first appeared, followed by the formation of Cl vacancies. Therefore, a BiOCl model containing one I-substitution defect was constructed and the formation energy (E_f) of Cl vacancies at different positions was calculated (Fig. 2e). The results show that the E_f value of Cl vacancy adjacent to the I-substitution defect is the lowest. According to the definition of E_f, the model with lower E_f value should be more preferable in energy, thus BOC-D_IV_{Cl} structures tend to form adjacent dual defects rather than isolated I-substitution defects and Cl vacancies. In order to further elucidate the uniqueness of the dual defect structure, we also explored the possibility of the occurrence of triple defects (Fig. 2f). According to theoretical calculations, when dual defects are formed, another Cl vacancy tends to appear in its non-adjacent positions, indicating that dual defects have thermodynamic stability advantages and can exist stably. In addition, this calculation result also explains the reason for the lower concentration of Cl vacancies in BOC-D_IV_{Cl}. The presence of dual defects inhibits the detachment of adjacent Cl atoms, macroscopically strengthening the halogen layer structure, resulting in a relatively lower concentration of Cl vacancies. Combining experiments and theoretical calculations, it can be determined that the existence of dual defect in BOC-D_IV_{Cl}.

In order to further clarify the type of halogen layer defect as the only structural difference, we compared the stress and torque differences of sample structural molecules by analyzing potential strain effects. In this work, Williamson-Hall (W-H) method was used to study the micro-strain according to the XRD peaks analysis [41]. Fig. S9 displays the uniform deformation (UDM) model plotting of the equation: $\beta_{hkl} \cdot cos\theta = k\lambda/D + 4\varepsilon \cdot sin\theta$, with the term ($4sin\theta$) along X-axis and ($\beta_{hkl} \cdot cos\theta$) along Y-axis corresponding to the XRD peaks of the samples [42]. The slope of the fitting line provides the strain effect value and the correlation co-efficient value R^2. It can be observed that all samples have similar strain effects and correlation co-efficient value, suggesting that the molecules in the sample have similar stress and torque, which excludes possible differences in molecular spatial stress behavior caused by defect differences. In short, we characterized the differences in defect

structures while excluding potential other differences in structural and molecular properties of the samples, which is crucial for studying the correlation between defect structures and O_2 activation characteristics.

3.2. Selective O_2 activation

To evaluate the O_2 activation process and disclose the dual defects effect for improved $^1O_2$ generation performance, systematic characterizations were carried out, including 3,3',5,5'-tetramethylbenzidine (TMB) oxidation analysis, molecular probe testing and ESR trapping measurement. The time-dependent absorption spectra of TMB oxidation reveal the highest O_2 activation ability of BOC-D_IV_{Cl}, indicating that dual defects have a greater advantage in improving the photocatalytic oxidation performance of BiOCl compared to single type defect (I-substitution defects or Cl vacancies) (Fig. 3a). To clarify the types of effective ROS during oxidation process, four scavengers (superoxide dismutase (SOD), L-histidine, catalase and mannitol) were introduced into the reaction system, which can specifically quench for $\cdot O_2^-$, $^1O_2$, H_2O_2 and $\cdot OH$. Fig. S10 reveals that SOD and mannitol can dramatically reduce the oxidation capacity for BOC-D_IV_{Cl}, manifesting $\cdot O_2^-$ and $^1O_2$ served as the primary ROS. Due to the fact that $^1O_2$ come from the oxidation of $\cdot O_2^-$, the similar attenuation of oxidation performance after both ROS quenching indicates that the production of high concentration $^1O_2$ is the key to achieving high oxidation activity, while the essence of $\cdot O_2^-$ quench is to inhibit the formation of $^1O_2$. This result suggests that the main reason for BOC-D_IV_{Cl} possess the optimal oxidation ability is that it produces more $^1O_2$. Furfuryl alcohol (FFA) probe experiment was also conducted to confirm the concentration difference of $^1O_2$ generated by the samples [43]. Fig. 3b exhibits that the concentration of FFA in the presence of BiOCl samples was greatly reduced and its loss amount followed the order BOC-D_IV_{Cl} > BOC-D_I > BOC-V_{Cl} > BOC, implying the highest formation amount of $^1O_2$ in BOC-D_IV_{Cl} system, which was further verified by ESR trapping measurements (Fig. 3c). By fitting the loss process of FFA, we quantified the steady-state yield and yield of $^1O_2$ (Fig. 3d), and confirmed that the $^1O_2$ production capacity of BOC-D_IV_{Cl} is 1.8, 3.8, and 4.8 times that of BOC-D_I, BOC-V_{Cl}, and BOC, respectively.

Furthermore, we compared the generation of $\cdot O_2^-$, H_2O_2 and $\cdot OH$ in
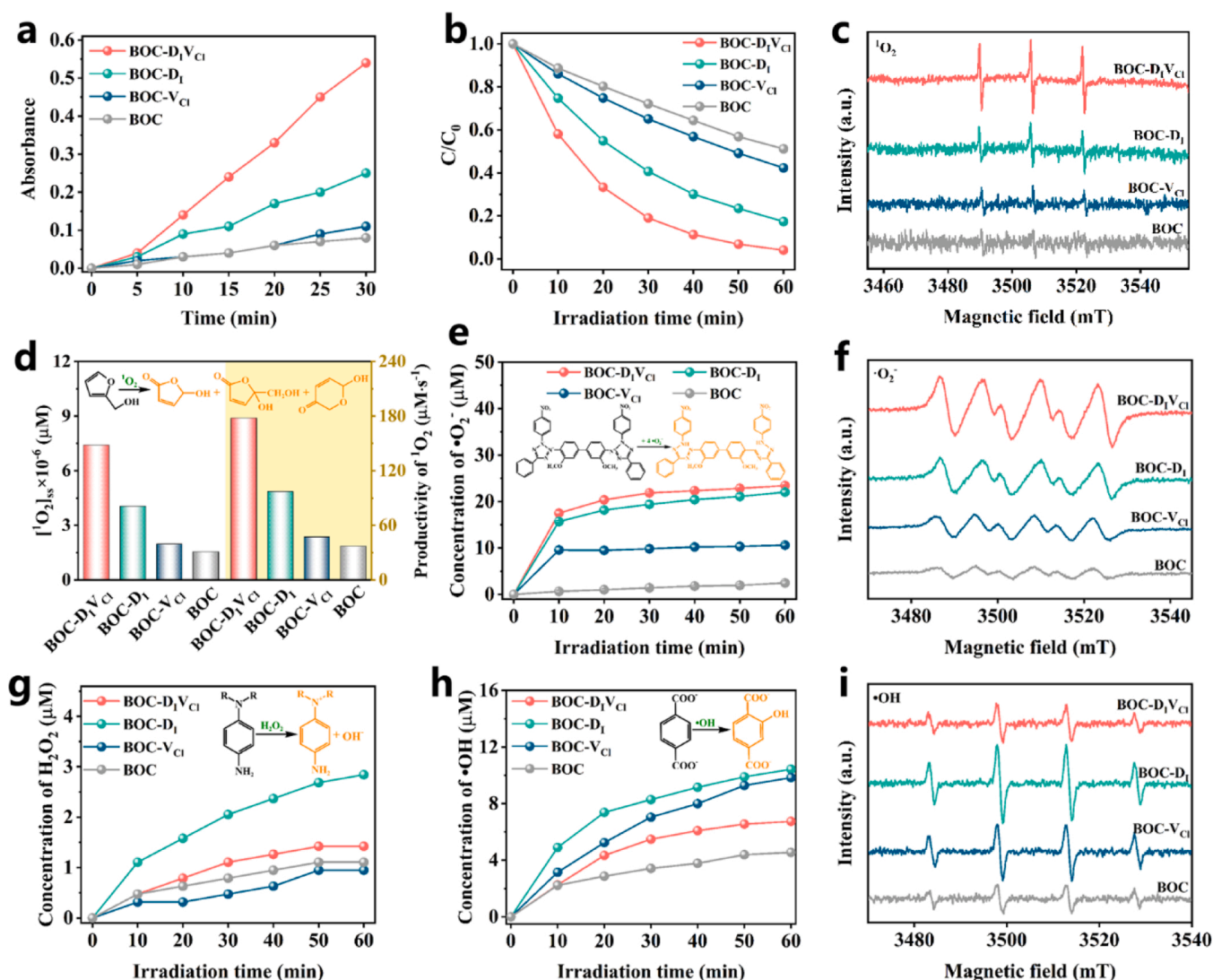
Fig. 3. (a) Time-dependent absorption spectra of TMB oxidation by the samples; (b) the proportion of FFA loss during continuous reaction time; (c) DMPO-ESR spectra for 10 min for $^1O_2$; (d) the steady-state concentration and production rate of $^1O_2$; (e) quantitative detection of $\bullet O_2^-$ over the samples; (f) DMPO-ESR spectra for 10 min for $\bullet O_2$; (g) time profiles of H_2O_2 generation for the samples; (h) quantitative detection of $\bullet OH$ over the samples; (i) DMPO-ESR spectra under visible light irradiation for 10 min for $\bullet OH$. All reactions are completed under visible light irradiation ($\lambda_{ex} \geq 420$ nm).

all catalyst system. The nitrotetrazolium blue chloride (NBT) molecular probe experiments (Fig. 3e) and ESR trapping tests (Fig. 3f) determined that BOC-D$_I$V$_{Cl}$ produces the highest amount of $\bullet O_2^-$, which means it has the potential to generate high concentrations of other types of ROS. However, under continuous light irradiation, the H_2O_2 generation ability of BOC-D$_I$V$_{Cl}$ is slight weaker than that of BOC-D$_I$ (Fig. 3g). A similar situation also occurs in the production of $\bullet OH$. As a molecular probe for confirming the concentration of $\bullet OH$, the lower attenuation of terephthalic acid (TPA) indicates that BOC-D$_I$V$_{Cl}$ produces a lower concentration of $\bullet OH$ than BOC-D$_I$ and BOC-V$_{Cl}$ (Fig. 3h). ESR trapping measurement provides additional evidence for the lower concentration of $\bullet OH$ by BOC-D$_I$V$_{Cl}$ (Fig. 3i). Based on the results above, it can be concluded that dual defects optimize the selectivity of $\bullet O_2^-$ conversion, exacerbating the generation of $^1O_2$.

3.3. Efficient purification of refractory aromatic pollutant induced by $^1O_2$

Benefiting from the enhanced O_2 activation ability for $^1O_2$ generation, BOC-D$_I$V$_{Cl}$ was considered to be an efficient photocatalyst for degradation of organic pollutants in deionized water. In this work, a series of aromatic pollutants commonly detected in surface water were

selected to evaluate photocatalytic performance. The degradation ratio (η) of pollutants is defined using η (%) = (1 - C/C$_0$) $\times$ 100%, where C and C$_0$ represent the pollutant concentrations in the effluent and the feeding stream, respectively. Selected the catalytic BPA reaction as an example, it can be seen that no obvious degradation of BPA in the absence of the photocatalysts nor in the presence of the photocatalysts but without visible light irradiation, which discloses that the decrease in BPA concentration is entirely derived from photocatalysis progress (Fig. S11). Fig. 4a exhibits that under continuous visible light irradiation, the degradation efficiencies of BOC-D$_I$V$_{Cl}$ for is superior to other catalysts, indicating its excellent photocatalytic performance. To confirm that high yield of $^1O_2$ is the main reason for outstanding photocatalytic performance, a quenching experiment was conducted. Adding L-histidine to the reaction systems, it is found that the degradation efficiency of BOC-D$_I$V$_{Cl}$ significantly decreased, while the degradation efficiency of another catalyst showed weak changes (due to the low photodegradation efficiency of BOC and BOC-V$_{Cl}$ on BPA, only BOC-D$_I$ was used as a reference sample for determination), confirming that the efficient pollutant removal efficiency originated from the generation of $^1O_2$ (Fig. 4b). The analysis of total organic carbon (TOC) confirms the efficient mineralization of pollutants by $^1O_2$ (Fig. 4c). Moreover, the
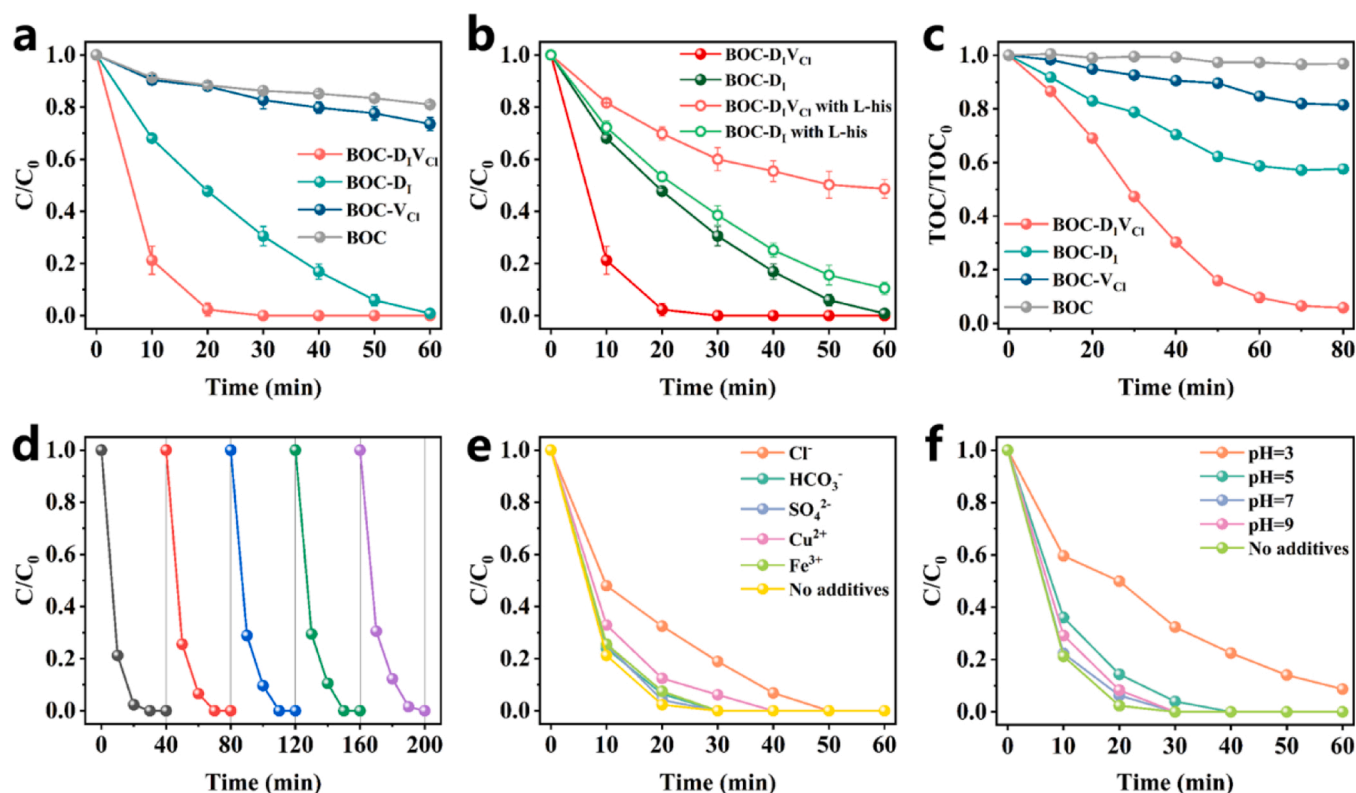
Fig. 4. (a) Photodegradation of BPA with the samples; (b) photodegradation of BPA before and after $^1O_2$ quenching; (c) residual ratio of TOC; (d) cyclic catalytic performance; (e) photodegradation efficiency of BPA by BOC-D_IV_{Cl} under different hydration conditions. The concentration of anions and cations are 0.1 mg·L^{-1}. All added substances did not cause significant changes in the pH of the solution, with a pH range of 6.9 ± 0.07. (f) photodegradation efficiency of BPA by BOC-D_IV_{Cl} under different pH. Error bars represent ± one standard deviation from the mean (n = 3).

degradation pathway was revealed by liquid chromatography-mass spectroscopy (LC-MS) analysis, and a degradation pathway was proposed (Fig. S12). In addition to BPA, we also compared the degradation performance of the catalyst for phenol, tetracycline and doxycycline hydrochloride. As shown in Fig. S13-15, the degradation efficiency of BOC-D_IV_{Cl} has always been superior to other catalysts, which not only confirms its excellent photocatalytic activity, but also indicates that the reaction driven by $^1O_2$ is applicable to the purification of various pollutants.

As a promising participant in photocatalysts, the photodegradation efficiency of BOC-D_IV_{Cl} for BPA was examined over five cycles, proving its stability and durability (Fig. 4d). In addition, we investigated the change of photocatalyst activity in the presence of cations (Cu^{2+} and Fe^{3+}) and anions (Cl^-, HCO_3^- and SO_4^{2+}). As shown in Fig. 4e, the photodegradation rate of BOC-D_IV_{Cl} on BPA under different hydration conditions is similar to that in deionized water, meaning that the process of producing $^1O_2$ induced by dual defects has good environmental adaptability. Finally, the degradation performance of BOC-D_IV_{Cl} on BPA at different pH was also detected, further confirming its potential application in real water quality (Fig. 4f). In summary, it has been confirmed that BOC-D_IV_{Cl}, with $^1O_2$ as the main ROS, not only exhibits excellent photocatalytic degradation efficiency for refractory organic compounds, but also has broad water quality applicability.

3.4. $^1O_2$ production mechanism of BOC-D_IV_{Cl}

To elucidate the origin of the enhanced photocatalytic $^1O_2$ generation, two elementary processes namely adsorption and activation of O_2, and selective conversion of $•O_2^-$ are taken into consideration. We first explored the adsorption characteristics of O_2 on the samples, which is the first step in the formation of $•O_2^-$. The adsorption energy (E_{ads}) of O_2 on different surface of the samples were calculated, and it was found that

dual defects, I-substitution defects and Cl vacancies become the O_2 adsorption sites on the surface of BOC-D_IV_{Cl}, BOC-D_I and BOC-V_{Cl}, respectively. As shown in Fig. 5a, all three types of defect have a promoting effect on the adsorption of O_2, which should come from the increase in electron density caused by unsaturated coordination bonds, providing convenience for the adsorption of O_2. Among them, O_2 has the smallest E_{ads} value on BOC-D_IV_{Cl} surface, indicating that the halogen layer modified by dual defect is more likely to adsorb O_2. The work function (W) data provide additional evidence that the adsorption effect of BOC-D_IV_{Cl} to O_2 is stronger than that of others. Dual defects can increase the surface potential and betatopic ability, thus obtaining strong coupling between BOC-D_IV_{Cl} with O_2. O_2-TPD verified the above conclusion from experimental perspective. The higher adsorption capacity in the low-temperature region (< 300 °C) confirms its better O_2 adsorption performance (Fig. 5b).

The adsorbed O_2 will combine with photo-generated electrons to form $•O_2^-$. To clarify the O_2 activation process, the understanding of abundance and kinetic behavior of photo-generated electrons is required. Therefore, we investigated the band structure and the microscopic behavior of photo-generation of the samples. UV–vis absorption spectra (Fig. S16) shows that all the introduction of three types of defects cause wider range of photoresponsive. The calculation of the density of states (DOS) indicates that the change in band structure originates from the difference in defect (Fig. 5c). The appearance and change of defects cause the formation and change of defect energy levels, which in turn leads to changes in the charge energy density on the valence band maximum (VBM) and conduction band minimum (CBM). The detailed band structure (Fig. S17) was estimated by Kubelka-Munk plot (Fig. S18) and XPS valence spectra (Fig. S19). Based on the light absorption characteristics and band structure changes of the samples, it can be determined that dual defects and I-substitution defects have greater regulatory effect than Cl vacancies. It should be noted that the
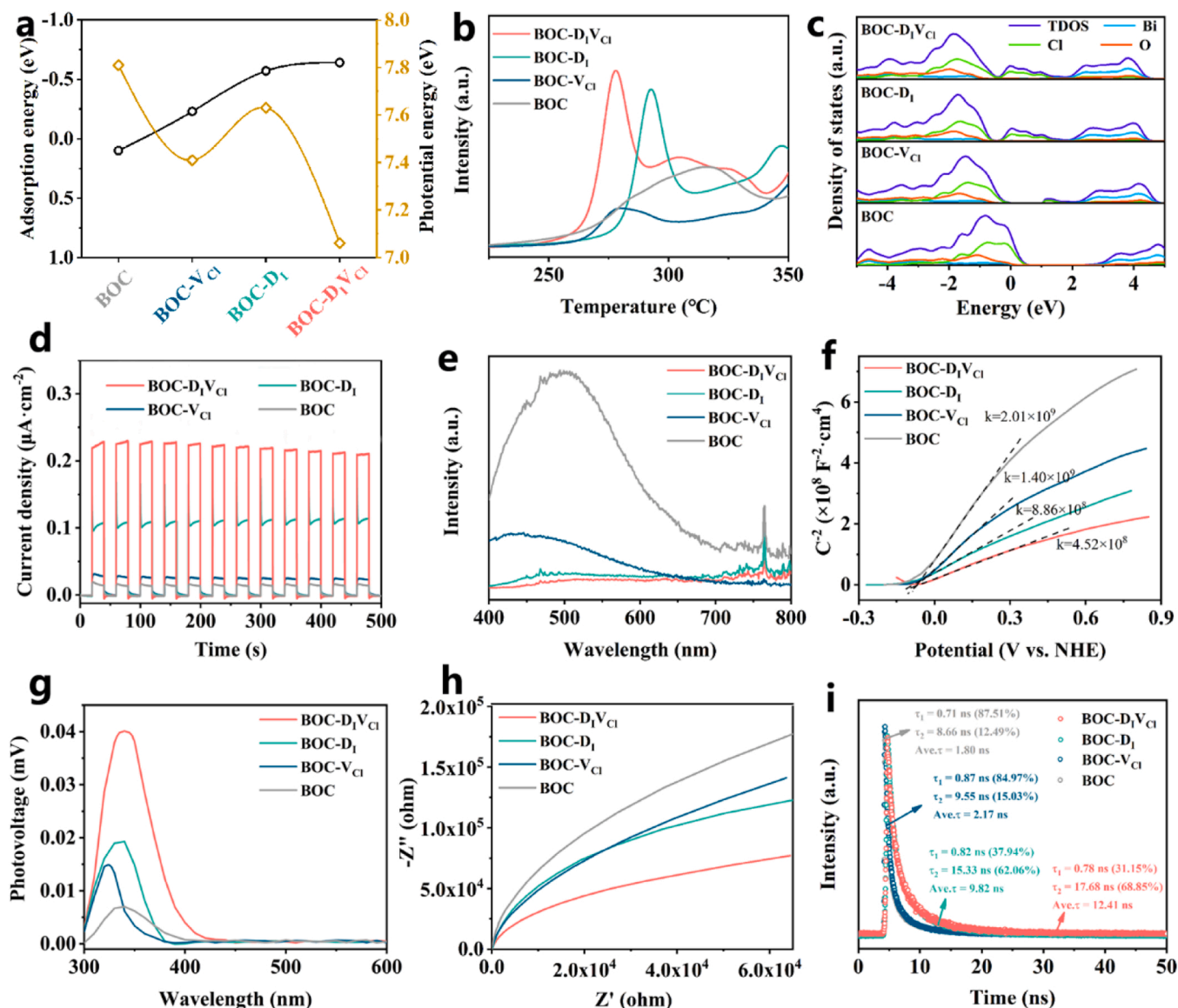
Fig. 5. (a) Calculated O_2 adsorption energy and electrostatic potential of the samples; (b) O_2-TPD profiles; (c) calculated DOS for the samples, the Fermi level is set to 0 eV; (d) TPC curves, (e) PL spectra ($\lambda_{ex} = 276$ nm), (f) Mott-Schottky plots, (g) stead-state SPV spectra, (h) EIS Nyquist plots and (i) time-resolved PL spectra of the samples.

bandgap of BOC-V_{Cl} is only slightly lower than that of BOC, but it is still difficult to absorb visible light, which may be the main reason for its significantly lower photocatalytic activity than BOC-D_IV_{Cl} and BOC-D_I. Further comparison was made between these two advantageous defects, and it is found that although I-substitution defects can induce further bandgap shortening, the return is only the harvesting of low energy photons, which are difficult to participate in O_2 activation reactions [44]. Meanwhile, a narrower bandgap will also exacerbate the coincidence of photogenerated charges, which is detrimental to the efficiency of the entire photocatalytic reaction [45].

In addition, the change in band structure is accompanied by a change in carrier dynamic properties. Here, the photoelectrical responses of the samples were compared. Fig. 5d shows the photocurrent density of BOC-D_IV_{Cl} is approximately 2.7, 8.1 and 9.6 times that of BOC-D_I, BOC-V_{Cl} and BOC, respectively. Therefore, BOC-D_IV_{Cl} has the greatest photoexcitation capability, which was corroborated by steady-state PL measurements showing the lowest PL quantum yield of BOC-D_IV_{Cl} (Fig. 5e). Such drastic PL quenching also reflects BOC-D_IV_{Cl} has the highest efficiency in photogenerated charge separation among the samples. Mott-

Schottky plots (Fig. 5f) demonstrate a higher charge density of BOC-D_IV_{Cl} (2.69×10^{22} cm³) than that of BOC-D_I (1.37×10^{22} cm³), BOC-V_{Cl} (8.71×10^{21} cm³) and BOC (6.05×10^{21} cm³). Meanwhile, stead-state SPV spectroscopy in Fig. 5g display BOC-D_IV_{Cl} has a stronger peak intensity than the others. These two sets of data further confirming the optimal induction effect of dual defects on the separation efficiency of photogenerated charges. The charge transfer properties were determined by EIS. It can be seen from Fig. 5h that the interface transfer impedance (R_{ct}) of both BOC-D_I and BOC-V_{Cl} are slight smaller than that of BOC, while meaningfully larger than that of BOC-D_IV_{Cl}, presenting that dual defects have significant advantages in regulating charge transfer performance compared to I-substitution defects or Cl vacancies. In addition to dynamic behavior, the influence of dual defects on the lifetime of photogenerated charges is also beneficial. Time-resolved PL spectroscopy in Fig. 5i indicates that PL decay process for BOC-D_IV_{Cl} is the slowest among the samples, and that for BOC is the fastest. By using a double-exponential model ($I = A_1\exp(-t/\tau_1) + A_2\exp(-t/\tau_2)$) to fit the PL decay curve [46], it can be found that the mechanism of extending the lifetime of photogenerated charges induced by dual defects lies in

increasing the proportion of indirect recombination of charge carriers. That is to say, dual defects enhance the chaos of photogenerated electron and hole migration, and this chaotic migration mode effectively improves the lifetime of photo-generated charges and provides convenient conditions for the combination of electrons and O_2. In addition, compared to BOC, the fact that higher photogenerated charge separation efficiency, charge migration rate, and more surface O_2 adsorption amount of BOC-D_I and BOC-V_{Cl} also explain the reason why they have higher concentration of ROS generation.

The binding ability of adsorbed O_2 to electrons is another key factor in evaluating the activation trend. The calculation of Bader effective charge (Δq) approves that O_2 can acquire 0.78 electrons from BOC-$D_I V_{Cl}$, versus only 0.73 electrons, 0.71 electrons and 0.61 electrons obtained from BOC-D_I, BOC-V_{Cl} and BOC, respectively (Fig. 6a). The significant electron binding advantage may be attributed to the unique adsorption configuration. Calculation results show that the most stable adsorption state of O_2 on the surface of BOC-$D_I V_{Cl}$ is Griffiths-type ("side-on" configuration), while the optimal state on the surface of the other samples is Pauling-type ("end-on" configuration) [47,48]. It can be seen from Fig. 6a that the "side-on" configuration shortens the distance between O_2 and the catalyst surface, making electron transfer easier, which facilitate the formation of $\bullet O_2^-$. Meanwhile, it is found that the O-O bond of O_2 on BOC-$D_I V_{Cl}$ surface was elongated, which may be due to the double coordination effect causing the spatial configuration distortion of the O_2. A longer O-O bond is also another factor that makes

it easier to activate. Overall, it can be confirmed that the dual defects have advantages in promoting O_2 adsorption, improving charge separation efficiency, and intensifying electron interface transport, which is the main reason for the generation of more $\bullet O_2^-$ in BOC-$D_I V_{Cl}$.

The influence of dual defects on $\bullet O_2^-$ conversion pathway was determined through theoretical calculations. In BOC, BOC-V_{Cl} and BOC-$D_I V_{Cl}$ catalytic systems, the thermodynamic conversion trend of pathway I is significantly higher than that of pathway II, as it requires less additional energy. However, the introduction of dual defects reversed this trend. As shown in Fig. 6b, the adsorption difficulty of the key intermediate $\bullet OOH$ in pathway I on the surface of BOC-$D_I V_{Cl}$ obvious increases, which rise the formation energy barrier of H_2O_2 and hinders the formation of H_2O_2 [49]. In addition, the energy change in the conversion process from $\bullet OOH$ to H_2O_2 in BOC-$D_I V_{Cl}$ system is very small, which means that the thermodynamic driving force of the reaction is insufficient. Due to the conversion of $\bullet O_2^-$ to H_2O_2 is a reversible reaction, a lower driving force of $\bullet OOH$ to H_2O_2 reaction may resulting in a large accumulation of $\bullet OOH$, increasing the likelihood of it being oxidized again to form $\bullet O_2^-$ it re-oxidized by holes, further weakening the probability of pathway I occurring [50]. Meanwhile, the $\bullet O_2^-$ accumulated in the reverse reaction once again become the raw materials for the formation of $^1O_2$, further promoting its formation. Therefore, one reason for dual defect induced $^1O_2$ generation can be confirmed to be that it increases the thermodynamic difficulty of the pathway I reaction.

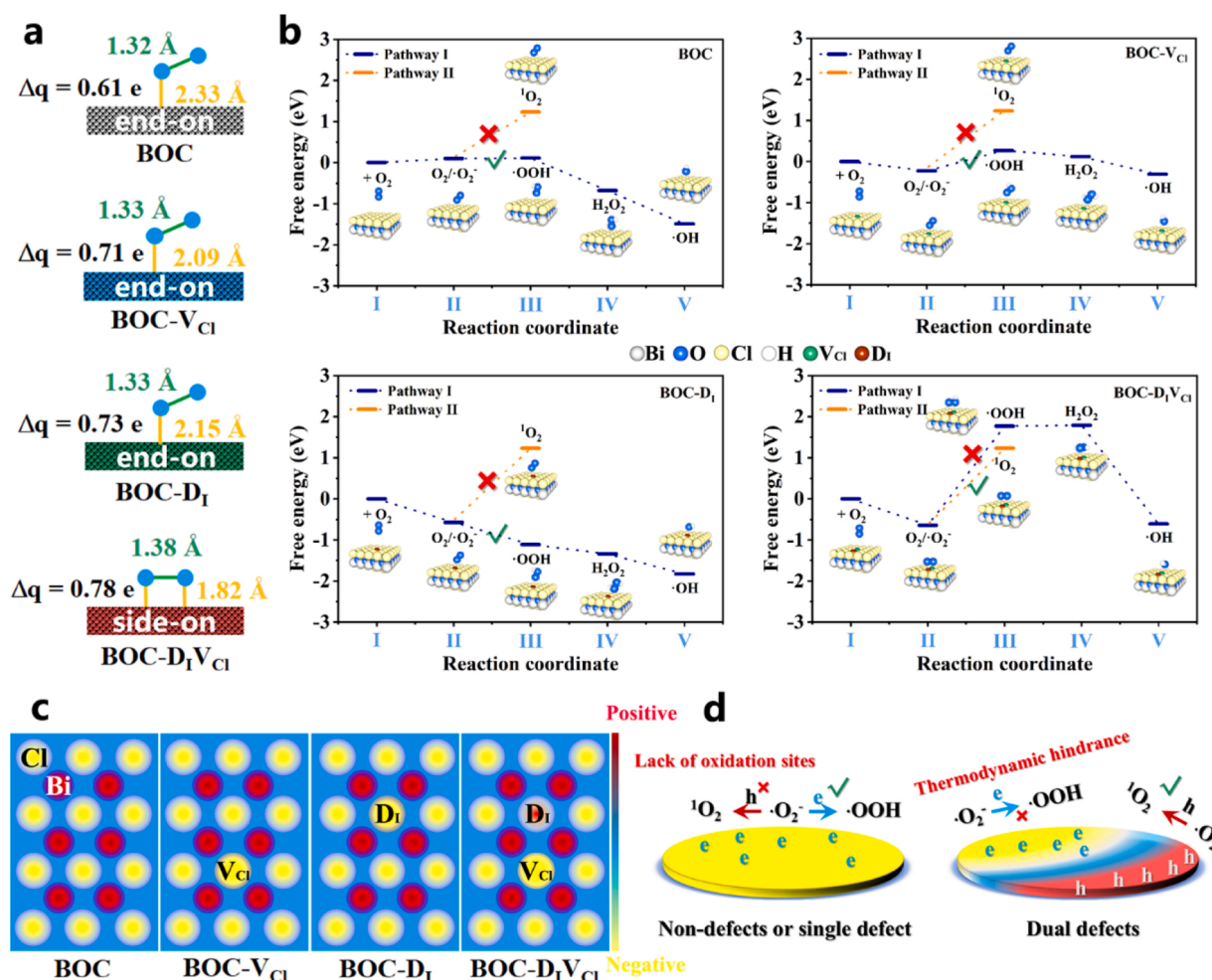The dual functional activation sites provided by dual defects may be

Fig. 6. (a) Schematic of the molecular O_2 pathway of "side-on" and "end-on" adsorption configuration on catalyst surface, and calculated bader effective charge (Δq) for the carried electrons of O_2 (positive means electrons depletion), O-O bond length of O_2 (green) as well as the distance between O_2 and catalyst surface (yellow); (b) Energy variation in O_2 adsorption and conversion processes; (c) charge distribution on (001) crystal facet; (d) schematic diagram of ROS transformation pathway differences caused by defect differences.

another reason for the selective transformation of ROS. Calculation results of charge density distribution indicate that both Cl vacancies in BOC-V_{Cl} and I-substitution defects in BOC-D_I serve as high electron density regions to provide electrons (Fig. 6c). As the dominant adsorption sites for O_2, these two defects will continuously provide electrons to promote the formation of $\bullet O_2^-$ and transform it along reaction pathway I. However, when the Cl vacancy adjacent to I-substitution defect forms, the role of I-substitution defects shifts from electron enriched sites to hole enriched sites, while dual defects become dual functional sites that can provide both electrons and holes. The O_2 with "side-on" adsorption configuration on dual defects can establish double channels to receive electrons and holes on the catalyst surface, thus possess an opportunity for conversion along pathway II after the formation of $\bullet O_2^-$. In comparison, the O_2 adsorption sites on the surface of single type defects and non-defect BiOCl can only provide electrons, and O_2 located in the high electron density region will continue to be attacked by electrons, making it tend to transition along pathway I (Fig. 6d).

4. Conclusion

In summary, we constructed a BOC-$D_I V_{Cl}$ nanostructure with dual defects (I-substitution defects and Cl vacancies) in halogen layer and investigated its photocatalytic O_2 activation performance. Experiment and theoretical calculation results show that the role of dual defects in improving the efficiency of photogenerated charge separation and enhancing O_2 adsorption performance of BiOCl is superior to that of I-substitution defects and Cl vacancies. More importantly, we confirmed that dual defects can promote the selective conversion of $\bullet O_2^-$ to $^1O_2$. Dual defects not only increase the thermodynamic difficulty of conversion of $\bullet O_2^-$ along pathway I ($\bullet O_2^- \rightarrow H_2O_2 \rightarrow \bullet OH$), but also provide oxidation-reduction bi-functional activation sites for the formation of $^1O_2$. Using BOC-$D_I V_{Cl}$ with excellent $^1O_2$ yield for the degradation of refractory aromatic pollutants in water, it was found that it has good application potential and broad environmental adaptability. This work is beneficial for understanding the essence of photocatalytic technology based on O_2 activation, and provide a new perspective for developing advanced strategies for environmental remediation.

CRediT authorship contribution statement

Han Weiguang: Formal analysis, Methodology. **Sun Yandong:** Formal analysis, Investigation, Methodology. **Li Hui:** Resources, Software. **Zhang Fangyuan:** Data curation, Formal analysis. **Zhang Xue:** Formal analysis. **Zhang Ziqi:** Formal analysis. **Shen Boxiong:** Software. **Ma Tianyi:** Conceptualization, Data curation, Investigation, Methodology. **Guo Sheng-Qi:** Conceptualization, Methodology.

Declaration of Competing Interest

The authors declare that they have no known competing financial interests or personal relationships that could have appeared to influence the work reported in this paper.

Data Availability

Data will be made available on request.

Acknowledgements

Appendix A. Supporting information

Supplementary data associated with this article can be found in the online version at doi:10.1016/j.apcatb.2023.123689.

References

[1] E. Romero, J.R. Gómez Castellanos, G. Gadda, M.W. Fraaije, A. Mattevi, Same substrate, many reactions: oxygen activation in flavoenzymes, Chem. Rev. 118 (2018) 1742–1769.
[2] Y. Shi, Z. Yang, L. Shi, H. Li, X. Liu, X. Zhang, J. Cheng, C. Liang, S. Cao, F. Guo, X. Liu, Z. Ai, L. Zhang, Surface boronizing can weaken the excitonic effects of BiOBr nanosheets for efficient O_2 activation and selective NO oxidation under visible light irradiation, Environ. Sci. Technol. 56 (2022) 14478–14486.
[3] N. Zheng, L. Li, X. Tang, W. Xie, Q. Zhu, X. Wang, Y. Lian, J. Yu, Z. Hu, Spontaneous formation of low valence copper on red phosphorus to effectively activate molecular oxygen for advanced oxidation process, Environ. Sci. Technol. 57 (2023) 5024–5033.
[4] W. Yang, K. Sun, J. Wan, Y. Ma, J. Liu, B. Zhu, L. Liu, F. Fu, Boosting holes generation and O_2 activation by bifunctional NiCoP modified $Bi_4O_5Br_2$ for efficient photocatalytic aerobic oxidation, Appl. Catal. B: Environ. 320 (2023) 121978.
[5] M.M. Montemore, M.A. Van Spronsen, R.J. Madix, C.M. Friend, O_2 activation by metal surfaces: implications for bonding and reactivity on heterogeneous catalysts, Chem. Rev. 118 (2018) 2816–2862.
[6] D. Zhang, Y. Li, P. Wang, J. Qu, S. Zhan, Y. Li, Regulating spin polarization through cationic vacancy defects in $Bi_4Ti_3O_{12}$ for enhanced molecular oxygen activation, Angew. Chem. Int. Ed. 62 (2023) e202303807.
[7] Q. Zhang, Y. Shi, X. Shi, T. Huang, S. Lee, Y. Huang, J. Cao, Constructing Pd/ferroelectric $Bi_4Ti_3O_{12}$ nanoflake interfaces for O_2 activation and boosting NO photo-oxidation, Appl. Catal. B: Environ. 302 (2022) 120876.
[8] B. An, Q. Zhang, B. Zheng, M. Li, Y. Xi, X. Jin, S. Xue, Z. Li, M. Wu, W. Wu, Sulfone-decorated conjugated organic polymers activate oxygen for photocatalytic methane conversion, Angew. Chem. Int. Ed. 61 (2022) e202204661.
[9] X. Cao, A. Huang, C. Liang, H.C. Chen, T. Han, R. Lin, Q. Peng, Z. Zhuang, R. Shen, H. Chen, Y. Yu, C. Chen, Y. Li, Engineering lattice disorder on a photocatalyst: photochromic BiOBr nanosheets enhance activation of aromatic C-, H. Bonds via Water Oxid., J. Am. Chem. Soc. 144 (2022) 3386–3397.
[10] T. Shen, X. Wang, J. Li, P. Xu, C. Yang, P. Wang, G. Zhang, Introduction of oxygen vacancy to $Bi_2Mn_4O_{10}$ supported by nickel foam for $^1O_2$ dominated metronidazole degradation under dielectric barrier discharge plasma, Appl. Catal. B: Environ. 328 (2023) 122518.
[11] Y. Shi, J. Li, D. Huang, X. Wang, Y. Huang, C. Chen, R. Li, Specific adsorption and efficient degradation of cylindrospermopsin on oxygen-vacancy sites of BiOBr, ACS Catal. 13 (2023) 445–458.
[12] H. Xu, X. Liu, H. Li, L. Zhang, O_2 activation and $^1O_2$ generation over phosphate modified BiOCl for efficient photodegradation of organic pollutants, Appl. Catal. B: Environ. 314 (2022) 121520.
[13] X. Chen, X. Zhang, Y. Li, M. Qi, J. Li, Z. Tang, Z. Zhou, Y. Xu, Transition metal doping BiOBr nanosheets with oxygen vacancy and exposed {102} facets for visible light nitrogen fixation, Appl. Catal. B: Environ. 281 (2021) 119516.
[14] X. Ma, X. Tang, Z. Hu, M. Zhen, B. Shen, S. Guo, F. Dong, Oxygen vacancies assist a facet effect to modulate the microstructure of TiO_2 for efficient photocatalytic O_2 activation, Nanoscale 15 (2023) 768–778.
[15] Y. Mao, P. Wang, L. Li, Z. Chen, H. Wang, Y. Li, S. Zhan, Unravelling the synergy between oxygen vacancies and oxygen substitution in BiO_{2-X} for efficient molecular-oxygen activation, Angew. Chem. Int. Ed. 59 (2020) 3685–3690.
[16] Q. Ren, Y. He, H. Wang, Y. Sun, F. Dong, Photo-switchable oxygen vacancy as the dynamic active site in the photocatalytic NO oxidation reaction, ACS Catal. 12 (2022) 14015–14025.
[17] S. Huang, F. Tian, J. Dai, X. Tian, G. Li, Y. Liu, Z. Chen, R. Chen, Highly efficient degradation of chlorophenol over bismuth oxides upon near-infrared irradiation: Unraveling the effect of Bi-O-Bi-O defects cluster and $^1O_2$ involved process, Appl. Catal. B: Environ. 298 (2021) 120576.
[18] W. Liu, P. Wang, J. Chen, X. Gao, H. Che, B. Liu, Y. Ao, Unraveling the mechanism on ultrahigh efficiency photocatalytic H_2O_2 generation for dual-heteroatom incorporated polymeric carbon nitride, Adv. Funct. Mater. (2022) 2205119.
[19] M. Li, S. You, X. Duan, Y. Liu, Selective formation of reactive oxygen species in peroxymonosulfate activation by metal-organic framework-derived membranes: a defect engineering-dependent study, Appl. Catal. B: Environ. 312 (2022) 121419.
[20] T. Pu, J. Ding, F. Zhang, K. Wang, N. Cao, E. Hensen, P. Xie, Dual atom catalysts for energy and environmental applications, Angew. Chem. Int. Ed. 62 (2023) e202305946.
[21] Q. Xia, J. Yang, S. Zhang, J. Zhang, Z. Li, J. Wang, X. Chen, Bodipy-based metal-organic frameworks transformed in solid stats from 1D chains to 2D layer structures as efficient visible light heterogeneous photocatalysts for forging C-B and C-C bonds, J. Am. Chem. Soc. 145 (2023) 6123–6134.
[22] J. Wang, M. Kuo, P. Zeng, L. Xu, S. Chen, T. Peng, Few-layer $BiVO_4$ nanosheets decorated with $SrTiO_3$: Rh nanoparticles for highly efficient visible-light-driven overall water splitting, Appl. Catal. B: Environ. 279 (2020) 119377.
[23] Y. Nosaka, A.Y. Nosaka, Generation and detection of reactive oxygen species in photocatalysis, Chem. Rev. 117 (2017) 11302–11336.

[24] H. Xia, H. Qin, Y. Zhang, H. Yin, Q. Li, F. Pan, D. Xia, D. Li, H. Xu, Modulate $^1O_2$ by passivate oxygen vacancy to boosting the photocatalytic performance of Z-scheme Mo_2S_3/BiOCl heterostructure, Sep. Purif. Technol. 266 (2021) 118547.

[25] H. Shang, M. Li, H. Li, S. Huang, C. Mao, Z. Ai, L. Zhang, Oxygen vacancies promoted the selective photocatalytic removal of NO with blue TiO_2 via simultaneous molecular oxygen activation and photogenerated hole annihilation, Environ. Sci. Technol. 53 (2019) 6444–6453.

[26] Q. Zhang, J. Chen, H. Che, B. Liu, Y. Ao, n→π* electron transitions and directional charge migration synergistically promoting O_2 activation and holes utilization on carbon nitride for efficiently photocatalytic degradation of organic contaminants, Small (2023) 2302510.

[27] L. Yu, H. Li, H. Shang, P. Xing, B. Zhou, Z. Chen, X. Liu, H. Zhang, Y. Shi, L. Zhang, Locally asymmetric BiOBr for efficient exciton dissociation and selective O_2 activation toward oxidative coupling of amines, ACS Nano 17 (2023) 15077–15084.

[28] G. Li, Z. Lian, Z. Wan, Z. Liu, J. Qian, Y. Deng, S. Zhang, Q. Zhong, Efficient photothermal-assisted photocatalytic NO removal on molecular cobalt phthalocyanine/Bi_2WO_6 Z-scheme heterojunctions by promoting charge transfer and oxygen activation, Appl. Catal. B: Environ. 317 (2022) 121787.

[29] Z. Sun, K. Sun, M. Gao, O. Metin, H. Jiang, Optimizing Pt electronic states through formation of a schottky junction on non-reducible metal-organic frameworks for enhanced photocatalysis, Angew. Chem. Int. Ed. 61 (2022) e202206108.

[30] Z. Zhang, M. Wang, F. Wang, Plasma-assisted construction of CdO quantum dots/CdS semi-coherent interface for the photocatalytic bio-CO evolution, Chem. Catal. 2 (2022) 1394–1406.

[31] J.P. Perdew, K. Burke, M. Ernzerhof, Generalized gradient approximation made simple, Phys. Rev. Lett. 77 (1996) 3865–3868.

[32] G. Kresse, J. Furthmuller, Efficient iterative schemes for ab initio total-energy calculations using a plane-wave basis set, Phys. Rev. B 54 (1996) 11169–11186.

[33] G. Kresse, J. Hafner, Ab initio molecular dynamics for open-shell transition metals, Phys. Rev. B 48 (1993) 13115–13118.

[34] L. Yang, S. Guo, Y. Chen, M. Pan, E. Ang, Z. Yuan, A mechanism investigation of how the alloying effect improves the photocatalytic nitrate reduction activity of bismuth oxyhalide nanosheets, ChemPhotoChem 4 (2020) 110–119.

[35] M. Guan, C. Xiao, J. Zhang, S. Fan, R. An, Q. Cheng, J. Xie, M. Zhou, B. Ye, Y. Xie, Vacancy associates promoting solar-driven photocatalytic activity of ultrathin bismuth oxychloride nanoshees, J. Am. Chem. Soc. 135 (2013) 10411–10417.

[36] Z. Luo, X. Ye, S. Zhang, S. Xue, C. Yang, Y. Hou, W. Xing, R. Yu, J. Sun, Z. Yu, X. Wang, Unveiling the charge transfer dynamics steered by built-in electric fields in BiOBr photocatalysts, Nat. Commun. (2022) 2230.

[37] W. Li, Y. Mao, Z. Liu, J. Zhang, J. Luo, L. Zhang, Z. Qiao, Chelated ion-exchange strategy toward BiOCl mesoporous single-crystalline nanosheets for boosting

[38] Z. Yang, Y. Shi, H. Li, C. Mao, X. Wang, X. Liu, X. Liu, L. Zhang, Oxygen and chlorine dual vacancies enable photocatalytic O_2 dissociation into monatomic reactive oxygen on BiOCl for refractory aromatic pollutant removal, Environ. Sci. Technol. 56 (2022) 3587–3595.

[39] Z. Cai, J. Merino, W. Fang, N. Kumar, J. Richardson, S. Feyter, R. Zenobi, Molecular-level insights on reactive arrangement in on-surface photocatalytic coupling reactions using tip-enhanced raman spectroscopy, J. Am. Chem. Soc. 144 (2022) 538–546.

[40] S. Guo, Z. Hu, M. Zhen, B. Gu, B. Shen, F. Dong, Insights for optimum cation defects in photocatalysis: a case study of hematite nanostructures, Appl. Catal. B: Environ. 264 (2020) 118506.

[41] S. Devesa, A. Rooney, M. Graca, D. Cooper, L. Costa, Williamson-hall analysis in estimation of crystallite size and lattice strain in $Bi_{1.34}Fe_{0.66}Nb_{1.34}O_{6.35}$ prepared by the sol-gel method, Mater. Sci. Eng. B 263 (2021) 114830.

[42] J. Zhang, B. Shen, Z. Hu, M. Zhen, S. Guo, F. Dong, Uncovering the synergy between Mn substitution and O vacancy in ZnAl-LDH photocatalyst for efficient toluene removal, Appl. Catal. B: Environ. 296 (2021) 120376.

[43] F. Lian, Y. Zhang, S. Gu, Y. Han, X. Cao, Z. Wang, B. Xing, Photochemical transformation and catalytic activity of dissolved black nitrogen released from environmental black carbon, Environ. Sci. Technol. 55 (2021) 6476–6484.

[44] E. Nikoloudakis, I. López-Duarte, G. Charalambidis, K. Ladomenou, M. Ince, A. Coutsolelos, Porphyrins and phthalocyanines as biomimetic tools for photocatalytic H_2 production and CO_2 reduction, Chem. Soc. Rev. 51 (2022) 6965–7045.

[45] S. Bagheri, A. TermehYousefi, T. Do, Photocatalytic pathway toward degradation of environmental pharmaceutical pollutants: structure, kinetics and mechanism approach, Catal. Sci. Technol. 7 (2017) 4548–4569.

[46] S. Guo, B. Yang, Z. Hu, M. Zhen, B. Gu, B. Shen, Uncovering mechanism of photocatalytic performance enhancement induced by multivariate defects on SnS_2, Nano Res 16 (2023) 2102–2110.

[47] A. Kulkarni, S. Siahrostami, A. Patel, J.K. Nørskov, Understanding catalytic activity trends in the oxygen reduction reaction, Chem. Rev. 118 (2018) 2302–2312.

[48] L. Xie, P. Wang, Y. Li, D. Zhang, D. Shang, W. Zheng, Y. Xia, S. Zhan, W. Hu, Pauling-type adsorption of O_2 induced electrocatalytic singlet oxygen production on N-CuO for organic pollutants degradation, Nat. Commun. 13 (2022) 5560.

[49] B. Yang, W. Wang, Z. Hu, B. Shen, S. Guo, Vacancy pairs regulate BiOBr microstructure for efficient dimethyl phthalate removal under visible light irradiation, J. Hazard. Mater. 458 (2023) 132008.

[50] T. Rajh, N.M. Dimitrijevic, M. Bissonnette, T. Koritarov, V. Konda, Titanium dioxide in the service of the biomedical revolution, Chem. Rev. 114 (2014) 10177–10216.